How to cite: *Angew. Chem. Int. Ed.* **2025**, *64*, e202501053
doi.org/10.1002/anie.202501053

Gas Separation

Ethylene Pretreatment Enhances Ethylene Adsorption and Separation over Cu@SAPO-RHO Zeolite

Ruobing Bai[+], *Nana Yan*[+], *Guangyuan He*[+], *Yingchun Ye, Risheng Bai, Dan Li, Peng Guo, Donghai Mei, Wenfu Yan,* and Jihong Yu**

Abstract: Efficient ethylene/ethane (C_2H_4/C_2H_6) separation using low-energy technologies is crucial for the chemical industry yet remains challenging due to the lack of industrially applicable adsorbents. Cu(I)-based adsorbents show significant potential; however, traditional synthesis methods often involve complex procedures or reduction steps. Herein, we report that Cu@SAPO-RHO zeolite, synthesized for the first time via a one-pot method with cyclam as the Cu(II) ligand, exhibits a remarkable C_2H_4/C_2H_6 selectivity of 22.6, a C_2H_4 uptake of 3.08 mmol g^{-1}, and a separation factor of 9.4 under ambient conditions by using a C_2H_4 pretreatment, placing it among the best-performing zeolitic materials. The C_2H_4 pretreatment enhances separation efficiency by partially reducing Cu(II) to Cu(I) and water resistance through the formation of carbon species during pretreatment. Structural analysis using Rietveld refinement reveals that Cu^{2+} ions occupy the corners of elliptical single 8-rings (*s8r*). X-ray absorption near-edge structure analysis confirms a reduction in the Cu oxidation state, while X-ray photoelectron spectroscopy corroborates the partial conversion of Cu(II) to Cu(I). Periodic density functional theory calculations further reveal that Cu(I) interacts more strongly with C_2H_4 than Cu(II). With its straightforward synthesis and enhanced performance through C_2H_4 pretreatment, Cu@SAPO-RHO zeolite presents a promising solution for industrial-scale C_2H_4/C_2H_6 separation.

Introduction

Ethylene (C_2H_4) is a fundamental building block in the chemical and petrochemical industries. It is predominantly produced through steam cracking or thermal decomposition of naphtha or ethane (C_2H_6), processes that inherently yield C_2H_6 as a byproduct.[1–3] However, efficient separation of C_2H_4 from C_2H_6 remains a significant industrial challenge due to their similar kinetic diameters and physicochemical properties.[4] Currently, cryogenic distillation is the standard method for C_2H_4 and C_2H_6 separation. This process requires extremely low temperatures (as low as 113 K) and high pressures, making it highly energy-intensive and costly.[5,6] To overcome these limitations, alternative low-energy separation technologies, such as membrane-based[7] and adsorptive separation methods,[8–11] have gained attention.

Adsorptive separation relies on mechanisms such as steric,[12–14] kinetic,[15] equilibrium,[16–18] or combinations thereof.[19,20] Advanced porous materials, including metal-organic frameworks (MOFs),[21] porous aromatic frameworks (PAFs),[22] and zeolites,[4,8] have shown promise for enhancing C_2H_4/C_2H_6 separation efficiency. Among these materials, zeolites are particularly attractive due to their high thermal and hydrothermal stability, excellent mechanical stability, tunable compositions, and low production cost, making them widely used in industrial separation processes.[4,8] Despite these advantages, porous adsorbents often face a trade-off between adsorption capacity and selectivity.[23] Practical adsorbents typically require a minimum adsorption capacity of 3 mmol g^{-1}[24] and a selectivity range of 5 to 70.[4] Breakthrough experiments assess separation performance via separation factors (or dynamic separation factors, which are defined as the maximum dynamic uptake ratio divided by the molar composition ratio in the feed gas), with values above 6 considered effective for C_2H_4/C_2H_6 separations.[4] Therefore, developing adsorbents that combine high C_2H_4 capacity and

---

[*] R. Bai[+], R. Bai, D. Li, D. Mei, W. Yan, J. Yu
State Key Laboratory of Inorganic Synthesis and Preparative Chemistry, College of Chemistry, Jilin University, Changchun 130012, China
E-mail: yanw@jlu.edu.cn
jihong@jlu.edu.cn

R. Bai[+], D. Li, J. Yu
International Center of Future Science, Jilin University, Changchun 130012, China

N. Yan[+], P. Guo
National Engineering Research Center of Lower-Carbon Catalysis Technology, Dalian Institute of Chemical Physics, Chinese Academy of Sciences, Dalian 116023, China

G. He[+], D. Mei
School of Materials Science and Engineering, Tiangong University, Tianjin 300387, China

Y. Ye
State Key Laboratory of Green Chemical Engineering and Industrial Catalysis, Sinopec Shanghai Research Institute of Petrochemical Technology Co., Ltd., Shanghai 201208, China

P. Guo
University of Chinese Academy of Sciences, Beijing 100049, China

[+] These authors contributed equally to this work.

Additional supporting information can be found online in the Supporting Information section selectivity under ambient conditions is essential for industrial applications.

In C_2H_4/C_2H_6 separations, the smaller kinetic diameter and higher quadruple moment of C_2H_4 enable steric, kinetic, or equilibrium-based separations.[9] Steric and kinetic mechanisms enhance selectivity through precise pore size and shape control but often compromise C_2H_4 uptake capacity.[9,25] In contrast, equilibrium-based separations rely on thermodynamically driven adsorbent–adsorbate interactions,[9] offering a more balanced trade-off. However, few equilibrium-based adsorbents—mainly select MOFs and PAFs[16,18,22]—have achieved both high C_2H_4 capacity and selectivity, highlighting the need for optimized zeolitic adsorbents. Previous studies reveal that unsaturated hydrocarbons can form π-complexation interactions with metal ions.[26,27] These interactions occur between the C═C bonds of olefins and the metal ions.[28,29] Examples include Cu(I)/Ag(I)Y,[30] Cu(I)NaX,[31] and AgZK-5[32] adsorbents. However, the high cost of Ag(I)-based materials limits their industrial feasibility, making Cu(I)-based adsorbents a more practical alternative. Unfortunately, conventional methods for synthesizing Cu(I)-based materials are complex and prone to contamination, presenting challenges for large-scale applications.

Cu(I)-based adsorbents are typically synthesized using two primary methods: 1) solid-solid exchange with CuCl, requiring an oxidant-free environment and thermal vacuum treatment,[33–35] and 2) reduction of Cu(II) precursors using various reducing agents such as vacuum[36,37] or inert gas[38] at high temperatures ($\geq$ 673 K) with precise control of residual carbon[37] and Cu species,[36,38] carbon monoxide (CO),[30] ammonia (NH_3),[39] hydrogen (H_2),[40] and methanol (CH_3OH) vapor.[41,42] Other reduction approaches utilize aqueous or solid-state reducing agents, such as Vitamin C,[43] sodium borohydride ($NaBH_4$),[44] and vanadium trichloride (VCl_3).[45] These methods demand stringent operating conditions, external reducing agents, and precise control over the resulting Cu species, complicating practical applications. Interestingly, studies have shown that C_2H_4 can act as a reducing agent. For example, Ni(II) in Ni-beta zeolite has been partially reduced to Ni(I) through in situ reaction with C_2H_4 at 393 K and 1 bar during C_2H_4 oligomerization.[46] Additionally, pretreatment strategies, such as precoking in methanol-to-olefins (MTO) reactions, have been successfully applied in industrial processes to enhance olefin selectivity and efficiency.[47–49] These findings suggest that a C_2H_4 pretreatment process could simplify the fabrication of Cu(I)-based adsorbents, eliminating external reducing agents and improving separation efficiency.

Here, we present Cu@SAPO-RHO, a silicoaluminophosphate (SAPO) **RHO** zeolite synthesized via a one-pot method for the first time by using cyclam as the Cu(II) ligand. Following a simple C_2H_4 pretreatment, this material demonstrated exceptional performance for C_2H_4/C_2H_6 separation, with a C_2H_4 adsorption capacity of 3.08 mmol g^{-1}, a selectivity of 22.6, and a dynamic separation factor of 9.4 under ambient conditions. The enhanced separation performance is attributed to the partial reduction of Cu(II) to Cu(I), as confirmed by X-ray absorption near-edge structure (XANES) and X-ray photoelectron spectroscopy (XPS). Periodic density functional theory (DFT) calculations revealed that Cu(I) exhibits a stronger adsorption affinity for C_2H_4 than Cu(II). These findings highlight the potential of Cu@SAPO-RHO as a highly effective and practical candidate for industrial C_2H_4/C_2H_6 separations. Furthermore, the C_2H_4 pretreatment process offers a streamlined and energy-efficient approach for fabricating Cu(I)-based adsorbents, paving the way for more sustainable and efficient separation technologies.

Results and Discussion

Synthesis and Characterization

M@SAPO-RHO zeolites (M = Cu, Ni, or Zn) were successfully synthesized for the first time using cyclam as the metal-ligand via a one-pot hydrothermal method. The synthesis utilized diethylamine (DEA), cetyltrimethylammonium bromide (CTAB), an M-cyclam solution, and SAPO-RHO seeds,[50,51] following a molar composition of 2.4 DEA: 1.0 Al_2O_3: 1.0 P_2O_5: 0.6 SiO_2: 100 H_2O: 10% seed (10 wt% of SiO_2): 0.03 CTAB: 0.1 M-cyclam (Figure 1a). The Cu-containing zeolite, designated as Cu@SAPO-RHO (or 0.1Cu@SAPO-RHO, where 0.1 refers to 0.1 Cu: Al_2O_3 ratio in the initial gel during synthesis), underwent C_2H_4 pretreatment, resulting in the modified material Cu@SAPO-RHO-P (Figure 1a).

Powder X-ray diffraction (PXRD) (Figure 1b and Figure S1) and scanning electron microscopy (SEM) (Figure S2) analyses confirmed the high crystallinity of both M@SAPO-RHO and Cu@SAPO-RHO-P. These samples exhibited uniform crystal sizes of approximately 10 µm. Nitrogen (N_2) adsorption/desorption isotherms measured at 77 K (Figure 1c and Figure S3) indicated high Brunauer–Emmett–Teller (BET) surface areas and substantial micropore volumes (Table S1). However, C_2H_4 pretreatment led to a slight decrease in both BET surface area and micropore volume for Cu@SAPO-RHO-P, likely due to the formation of carbon deposits during pretreatment.[52] Thermogravimetric (TG) analysis (Figure S4) and CHN elemental analysis (Table S2) confirmed an increase in carbon content (~1.8 wt%) after C_2H_4 pretreatment. This increase corroborates the incorporation of carbon species during pretreatment.

Ultraviolet–visible (UV–vis) spectroscopy (Figure S5) revealed characteristic absorption peaks corresponding to Cu(II) species in Cu@SAPO-RHO. Peaks at ~220 and ~253 nm were attributed to Cu^{2+} ions and CuO_x species, respectively, while the broad peak at 700–800 nm represented the d–d transition of Cu(II).[41,53]

The precise location of Cu ions in the Cu@SAPO-RHO framework was determined using Rietveld refinement against high-resolution PXRD data processed with TOPAS 5.0. This approach, previously used for determining the positions of organic structure-directing agents (OSDAs) and inorganic cations (e.g., Na^+, K^+, and Cs^+) in SAPO-**RHO** zeolites,[51,54] provided valuable insights into Cu ion placement. The SAPO-**RHO** zeolite initially crystallized in the $I432$ space

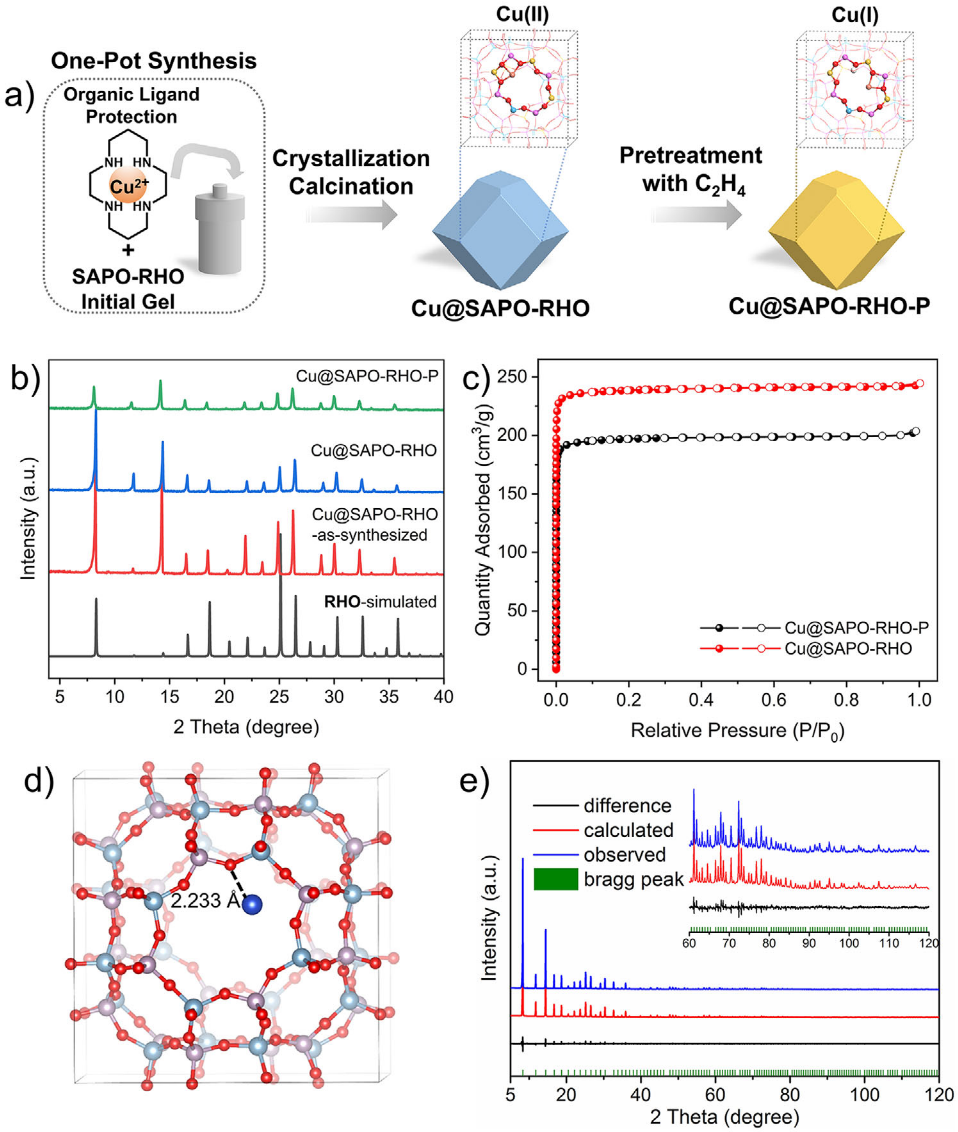

Figure 1. a) Schematic illustration of the synthetic process of Cu@SAPO-RHO and Cu@SAPO-RHO-P, b) PXRD patterns of Cu@SAPO-RHO before and after calcination and C_2H_4 pretreatment, c) N_2 adsorption/desorption isotherms of Cu@SAPO-RHO and Cu@SAPO-RHO-P at 77 K, d) crystallographic structure, and e) the final Rietveld refinement plots of Cu@SAPO-RHO. The observed, calculated, and difference curves are in blue, red, and black, respectively. The vertical bars indicate the positions of the Bragg peaks ($\lambda = 1.5406$ Å).

group but transitioned to the *I*23 space group after ion exchange.[51] This structural change resulted in elliptical eight-ring (*s*8*r*) pore openings (Figure S6). Consequently, the distorted SAPO-**RHO** framework in the *I*23 space group was used as the structural model for dehydrated Cu@SAPO-RHO.

A difference electron density map (Figure S6), derived from the experimental PXRD data, identified the preliminary positions of Cu^{2+} ions within the SAPO-**RHO** framework. The final refinement yielded satisfactory convergence, with Rp = 0.0476 (Table S3). The refinement results revealed that Cu^{2+} ions occupy the corners of the elliptical *s*8*r* in the SAPO-**RHO** framework. These ions are coordinated to framework oxygen (O) atoms, with the shortest Cu—O bond distance of 2.233 Å (Figure 1d,e).

Gas Adsorption and Separation Performance

The gas adsorption and separation capabilities of M@SAPO-RHO zeolites, including Cu@SAPO-RHO-P, were evaluated against several comparative samples. These samples included H-SAPO-RHO, Cu-SAPO-RHO, Cu-SSZ-13 (**CHA**), and Cu-SAPO-34 (**CHA**) prepared via conventional Cu^{2+} ion exchange, CuO/SAPO-RHO via wet impregnation, and Cu@SAPO-34 (**CHA**) synthesized using a one-pot method. All samples exhibited high crystallinity (Figure S1), uniform crystal sizes (Figure S2), and substantial BET surface areas and pore volumes (Figure S3 and Table S1).

The adsorption isotherms for C_2H_4 and C_2H_6 on Cu@SAPO-RHO and Cu@SAPO-RHO-P were measured at 298 K up to 1 bar (Figure 2a). C_2H_4 pretreatment significantly

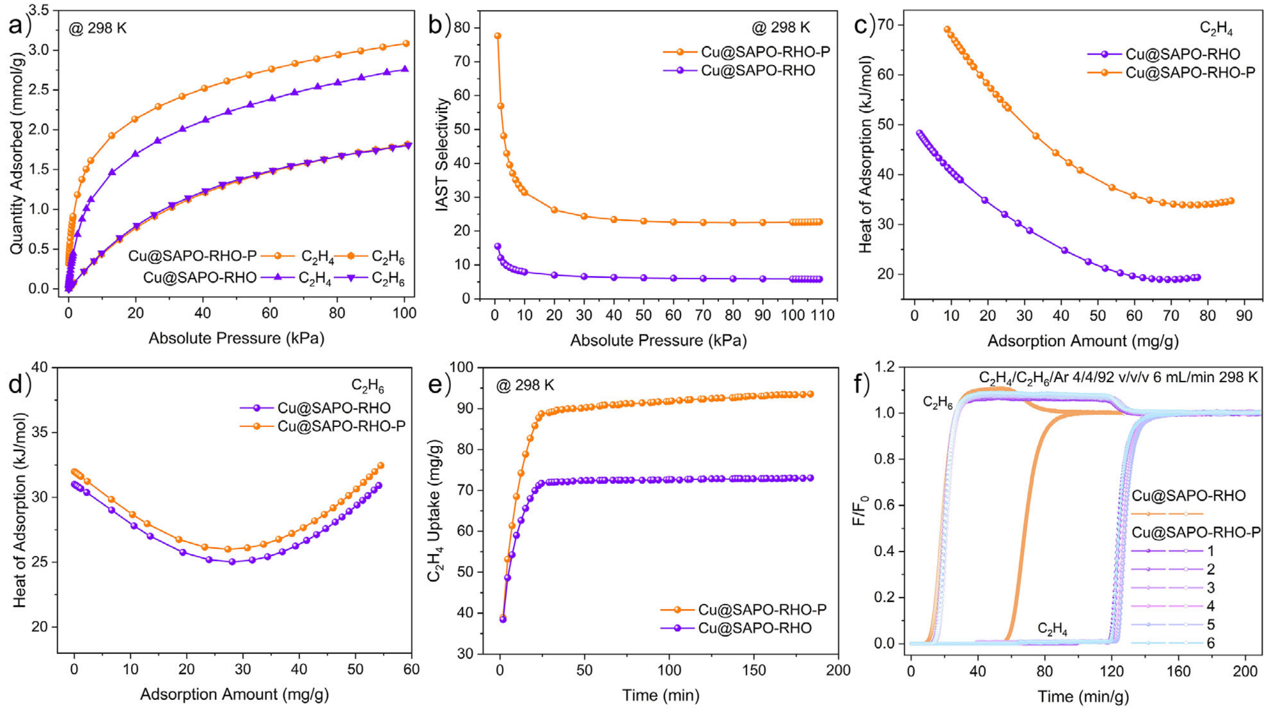

Figure 2. a) C_2H_4 and C_2H_6 adsorption isotherms at 298 K between 0 and 1 bar, b) C_2H_4/C_2H_6 (50/50, v/v) IAST selectivities at 298 K for Cu@SAPO-RHO and Cu@SAPO-RHO-P, the isosteric heat of adsorption of Cu@SAPO-RHO and Cu@SAPO-RHO-P at 298 K for c) C_2H_4 and d) C_2H_6, e) adsorption kinetic curves of C_2H_4 for Cu@SAPO-RHO and Cu@SAPO-RHO-P at 298 K and 1 bar, f) C_2H_4/C_2H_6/Ar (4/4/92, v/v/v, 6 mL min^{-1}) breakthrough curves for Cu@SAPO-RHO and Cu@SAPO-RHO-P at 298 K and 1 bar with regeneration at 573 K for 30 min.

enhanced the C_2H_4 adsorption capacity, increasing from 2.76 to 3.08 mmol g^{-1} (equivalent to 8.2 to 9.2 molecules per unit cell). In contrast, C_2H_6 adsorption remained nearly unchanged. Selectivity analysis using the ideal adsorbed solution theory (IAST) and dual-site Langmuir–Freundlich model (Figure 2b and Figures S7–S9) showed that the C_2H_4/C_2H_6 (50/50, v/v) selectivity for Cu@SAPO-RHO-P improved significantly, reaching 31.4 at 0.1 bar and 22.6 at 1 bar. These values surpassed those of other SAPO-RHO and **CHA** samples evaluated in this study (Figure S7).

The adsorption/desorption isotherms for C_2H_4 and C_2H_6 were measured at 273, 298, and 313 K between 0 and 1 bar (Figure S10), demonstrating the excellent desorption performance of Cu@SAPO-RHO-P. The adsorption isotherms were analyzed using the Virial equation (Table S4) to calculate the isosteric heat of adsorption (Q_{st}) (Figure 2 c,d and Figure S11). After C_2H_4 pretreatment, the Q_{st} for C_2H_4 increased from 48.3 to 69.1 kJ mol^{-1} at low loading (pressure value: 0.0003 bar), indicating stronger interactions with the Cu@SAPO-RHO-P framework. In contrast, the Q_{st} for C_2H_6 remained relatively constant. Compared to other samples, Cu@SAPO-RHO-P exhibited a significantly higher Q_{st} of C_2H_4, outperforming H-SAPO-RHO (43.0 kJ mol^{-1}), Cu-SAPO-RHO (40.5 kJ mol^{-1}), and CuO/SAPO-RHO (42.1 kJ mol^{-1}) (Figure S11). This enhanced interaction confirms the superior affinity of Cu@SAPO-RHO-P for C_2H_4 molecules.

The C_2H_4 adsorption kinetics of Cu@SAPO-RHO-P was significantly faster than that of untreated Cu@SAPO-RHO (Figure 2e). The diffusional time constant (D/r^2, where D is the diffusion coefficient, and r is the radius of the equivalent spherical particle),[55,56] calculated as 5.23×10^{-8} s^{-1} for Cu@SAPO-RHO-P, was significantly higher than the 3.51×10^{-9} s^{-1} observed for Cu@SAPO-RHO (Figure S12). This improvement demonstrates the role of C_2H_4 pretreatment in enhancing C_2H_4 adsorption performance.

Breakthrough experiments using a C_2H_4/C_2H_6/argon (Ar) mixture (4/4/92, v/v/v) confirmed the improved separation performance of Cu@SAPO-RHO-P under competitive adsorption conditions (Figure 2f and Figure S13). After pretreatment, the dynamic C_2H_4 uptake nearly doubled, increasing from 0.74 to 1.36 mmol g^{-1} (equivalent to 2.2 to 4.0 molecules per unit cell) at 0.04 bar. The separation factor also increased from 4.8 to 9.4, with a C_2H_4 retention time of 120 min g^{-1}. This performance was sustained over six fully regenerative breakthrough cycles. Cu@SAPO-RHO-P outperformed all other SAPO-RHO and **CHA** zeolites evaluated in this study, highlighting its potential for industrial-scale C_2H_4/C_2H_6 separation (Figures S14–S16).

For static adsorption at 1 bar, Cu@SAPO-RHO-P exhibited a slightly lower C_2H_4 uptake (3.08 mmol g^{-1}) compared to H-SAPO-RHO (3.45 mmol g^{-1}), likely due to reduced BET surface area after Cu incorporation[57] (Figure S8 and Table S1). However, at low pressures (< 0.06 bar), Cu@SAPO-RHO-P showed higher C_2H_4 uptake than H-SAPO-RHO (Figure S8). This trend was confirmed in breakthrough experiments, where Cu@SAPO-RHO-P achieved a dynamic C_2H_4 uptake of 1.36 mmol g^{-1} at 0.04 bar, compared to 1.27 mmol g^{-1} for H-SAPO-RHO (Figure 2f and Figure S16). These results highlight the strong affinity of Cu@SAPO-RHO-P for C_2H_4 at low partial pressures, making it a promising candidate for capturing low-concentration C_2H_4 in industrial applications.

Determination of Adsorption Affinity after Pretreatment

To investigate the role of Cu species in enhancing C_2H_4 adsorption and separation, xCu@SAPO-RHO zeolites with varying Cu contents (x = 0.01, 0.03, 0.06, 0.1) were synthesized (Table S1). All SAPO-RHO samples in this study underwent pretreatment with C_2H_4. PXRD analysis confirmed that the SAPO-RHO-P samples retained high crystallinity after pretreatment (Figure S1). Among the samples, Cu@SAPO-RHO-P showed improved separation performance, while other samples, such as Ni/Zn@SAPO-RHO-P and H-SAPO-RHO-P, exhibited reduced efficiency following C_2H_4 pretreatment. These results highlight the critical role of Cu species in achieving superior separation performance (Figures S15–S17).

TG analysis (Figure S4) and CHN elemental analysis (Table S2) indicated an increase in carbon species on all C_2H_4-pretreated samples. For Cu@SAPO-RHO-P, variations in pretreatment temperatures affected the carbon content. However, breakthrough experiments showed no consistent correlation between carbon content and enhanced C_2H_4 uptake (Figures S18 and S19). In contrast, H-SAPO-RHO-P, which contained more carbon species than untreated H-SAPO-RHO, showed reduced C_2H_4 uptake (Figure S15). This finding suggests that carbon species formed during pretreatment negatively impact separation efficiency in non-Cu-containing samples.

The type and quantity of Cu species played a significant role in determining separation performance. Samples with low Cu content confined in zeolite microenvironment, such as Cu-SAPO-RHO-P, CuO/SAPO-RHO-P, and 0.01Cu@SAPO-RHO-P, exhibited reduced separation efficiency after C_2H_4 pretreatment (Figure S15 and Figure S20). This reduction was attributed to insufficient Cu content ($\leq$ 0.1 Cu per unit cell; Table S1) to counteract the adverse effects of carbon species formed during pretreatment. In contrast, xCu@SAPO-RHO-P samples with higher Cu content per unit cell (0.4, 0.8, and 1.0 for x = 0.03, 0.06, and 0.1, respectively; Table S1) exhibited superior C_2H_4 adsorption and separation performance. Dynamic separation factors reached 7.6 and 8.3 for 0.03Cu@SAPO-RHO-P and 0.06Cu@SAPO-RHO-P, respectively (Figures S20 and S21). Although increasing Cu content reduced the BET surface area of xCu@SAPO-RHO precursors (Figure S3 and Table S1), C_2H_4 pretreatment selectively enhanced C_2H_4 adsorption. Among all samples, 0.1Cu@SAPO-RHO-P achieved the highest separation efficiency, with a dynamic separation factor of 9.4 (Figure S21).

A CO-pretreated sample, Cu@SAPO-RHO-PCO, was prepared using a CO/Ar mixture (5/95, v/v) at 673 K. This sample exhibited a C_2H_4 dynamic uptake of 1.21 mmol g^{-1} and a separation factor of 7.4 (Figure S18). However, when CO pretreatment was conducted at 573 K—the same temperature used for C_2H_4 pretreatment—the dynamic uptake decreased to 1.08 mmol g^{-1} (Figure S18). In comparison, pretreatment with a C_2H_4/Ar mixture (5/95, v/v) at 573 K resulted in superior results. The dynamic uptake reached 1.14 mmol g^{-1}, and the separation factor increased to 7.6 (Figure S18), surpassing the performance of the CO-pretreated sample at the same temperature. These results suggest that C_2H_4 serves as an effective reducing agent,[46] facilitating the reduction of Cu(II) species and thus enhancing the separation performance of Cu@SAPO-RHO.

Analysis of Cu Reduction after Pretreatment

To investigate the role of Cu reduction, XANES, and Fourier-transformed extended X-ray absorption fine structure (FT-EXAFS) analyses were conducted. XANES spectra of Cu@SAPO-RHO and Cu@SAPO-RHO-P (Figure 3a) showed increased pre-edge intensity (~8980 eV) and decreased white-line intensity (~8995 eV) following C_2H_4 pretreatment. These changes indicate a reduction in the oxidation state of Cu species.[58–61] FT-EXAFS spectra (Figure 3b) revealed a main peak in the first coordinated shell at 1.50 Å in R-space, corresponding to the Cu—O scattering path. The absence of a Cu—Cu scattering peak confirmed the presence of isolated Cu species.[62] Quantitative fitting of the Cu *K*-edge EXAFS spectra (Figure 3c and Figure S22) showed a decrease in the Cu—O coordination number (CN) from 3.01 in Cu@SAPO-RHO to 2.20 in Cu@SAPO-RHO-P (Table S5), further supporting the partial reduction of Cu(II) species.

XPS analysis also confirmed the reduction of Cu species after pretreatment. Before pretreatment, Cu species in Cu-containing samples primarily existed as Cu(II), with a minor fraction of Cu(I) (Figure 3d and Figure S23). An exception was CuO/SAPO-RHO, which contained only Cu(II) species. Similarly, Ni/Zn@SAPO-RHO exclusively contained divalent Ni and Zn species (Figure S23).[63–65]

The Cu $2p_{3/2}$ XPS spectra revealed peaks at 933.4 eV for Cu(I) and peaks at 935.4 eV for Cu(II), along with shake-up features at ~945.0 eV.[63,66,67] After C_2H_4 pretreatment, the diminished shake-up feature indicated a significant reduction in Cu(II) content (Figure 3d).[68] Quantitative analysis showed that the Cu(I) fraction increased from 34% to 80%, while Cu(II) content decreased from 66% to 20% (Figure 3e). Comparatively, Cu@SAPO-RHO-PCO, prepared via CO pretreatment, exhibited a Cu(I) content of 75% (Figure S23). These findings suggest that C_2H_4 is a more effective reducing agent than CO. This conclusion was also supported by the longer C_2H_4 retention time observed for Cu@SAPO-RHO-P relative to Cu@SAPO-RHO-PCO (Figure 2f and Figure S18).

xCu@SAPO-RHO-P samples (x = 0.03, 0.06) with lower Cu content also showed a significant increase in Cu(I) fraction after C_2H_4 pretreatment. The Cu(I) proportion increased from 26% to 82% for x = 0.03, and 33% to 88% for x = 0.06 (Figure S23). xCu@SAPO-RHO-P samples (e.g., x = 0.03, 0.06, 0.1), consistently showed higher Cu(I) fractions and better separation performance, as reflected in the separation factors (Figure S21).

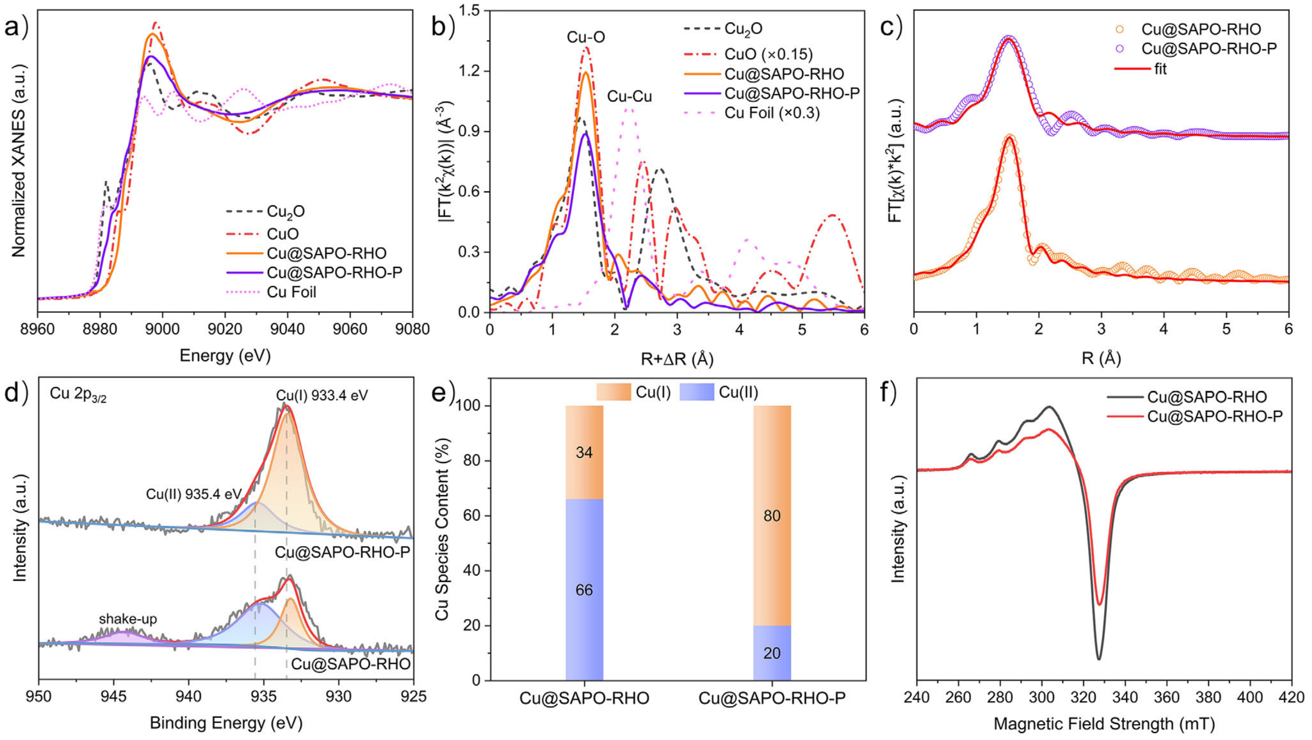

Figure 3. Characterization of Cu species in Cu@SAPO-RHO and Cu@SAPO-RHO-P. a) Normalized Cu K-edge XANES spectra, b) Cu K-edge FT–EXAFS spectra without phase correction, and c) EXAFS fitting curves of Cu K-edge. The Cu foil, Cu_2O, and CuO were used as references. d) Cu $2p_{3/2}$ XPS spectra, e) quantitative analysis of Cu(II) and Cu(I) species, and f) EPR spectra of Cu@SAPO-RHO and Cu@SAPO-RHO-P.

Electron paramagnetic resonance (EPR) spectroscopy further confirmed the reduction of Cu(II). The EPR spectra (Figure 3f) showed a significant decrease in the peak intensity at ~325 mT, corresponding to isolated Cu^{2+} sites.[69] This reduction in intensity was observed for both Cu@SAPO-RHO-P and Cu@SAPO-RHO-PCO (Figure S24), confirming the depletion of Cu(II) species.[70–72]

C_2H_4 plays a critical role in facilitating Cu(II) reduction, as the generation of H^+ (the likely charge-compensating species during pretreatment) is primarily attributed to the dehydrogenation of C_2H_4 through oxidative addition.[46] To better understand the adsorption mechanisms of C_2H_4 and C_2H_6 on Cu(I) and Cu(II) sites in the SAPO-**RHO** system, adsorption energies (E_{ads}) were calculated using DFT (Figure 4a–d and Figure S25). The results showed that C_2H_4 adsorption was stronger on **RHO**-Cu(I) (-215.9 kJ mol^{-1}) than on **RHO**-Cu(II) (-163.0 kJ mol^{-1}). For C_2H_6, the difference was smaller, with adsorption energies of -107.8 kJ mol^{-1} for **RHO**-Cu(I) and -99.6 kJ mol^{-1} for **RHO**-Cu(II). The larger C_2H_4/C_2H_6 adsorption energy difference for Cu(I) (108.1 kJ mol^{-1}) versus Cu(II) (63.4 kJ mol^{-1}) indicates higher selectivity for C_2H_4 adsorption on Cu(I) sites. Projected density of states (PDOS) analysis further supported these findings. According to *d*-band center theory,[73] transition metals with a higher *d*-band center relative to the Fermi level exhibit stronger bonding with adsorbates. For **RHO**-Cu(I) and **RHO**-Cu(II), the calculated *d*-band center (ε_d) was -1.27 and -1.76 eV, respectively (Figure 4e). The closer proximity of **RHO**-Cu(I)'s *d*-band center to the Fermi level explains its stronger affinity for both C_2H_4 and C_2H_6 compared to **RHO**-Cu(II).

Evaluation of Industrial Application Potential

The industrial applicability of Cu@SAPO-RHO-P was evaluated using breakthrough experiments to test its regeneration capability under various conditions (Figure 5a and Figure S26). The recovery of C_2H_4 after regeneration with 50 mL min^{-1} Ar for 30 min improved progressively with temperature: 74.81% at 298 K, 88.64% at 423 K, 95.62% at 493 K, and 100% at 573 K (Figure S27). With regeneration at 298 K, the C_2H_4 purity in the desorbed gas was estimated to be 99.01% (Figure S26). After ten breakthrough cycles (cycles 2–11, Figure 5b), the material maintained stable performance, including consistent dynamic uptake, retention time, and separation factor for C_2H_4. These results confirmed the excellent cyclic stability of Cu@SAPO-RHO-P.

Additional breakthrough experiments were conducted with feed gas mixtures containing impurities such as carbon dioxide (CO_2) and methane (CH_4). These experiments explored different conditions, including C_2H_4/C_2H_6 ratios (50/50, v/v) and C_2H_4/C_2H_6/Ar ratios (10/10/80 and 25/25/50, v/v/v), total flow rates (e.g., C_2H_4/C_2H_6/Ar at 4/4/92, v/v/v, at 12 and 18 mL min^{-1}), relative humidities (0% and 55% RH), and operating temperatures (298, 313, and 333 K) (Figure S28). Breakthrough cycles with a 50/50 C_2H_4/C_2H_6 mixture at 298 K further confirmed good cyclic performance

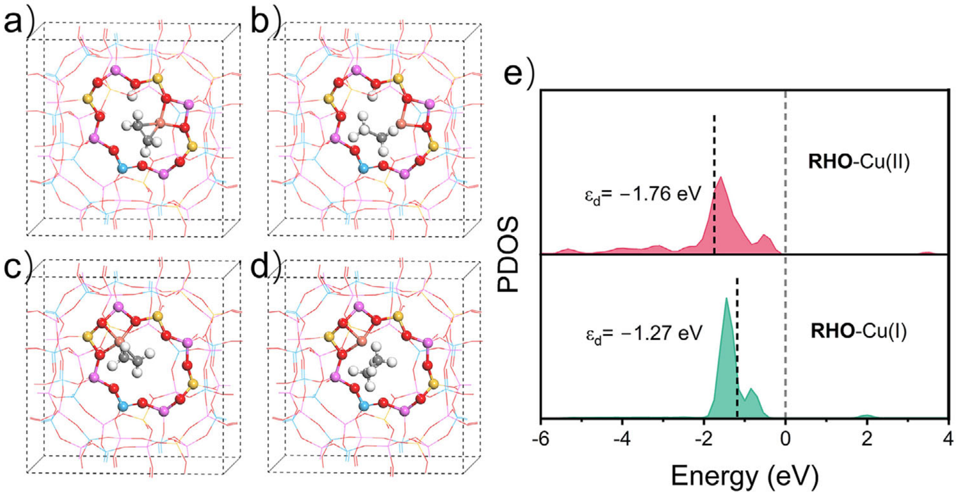

Figure 4. Adsorption configurations of C_2H_4 and C_2H_6 over a,b) **RHO**-Cu(I) and c,d) **RHO**-Cu(II) model systems, e) the PDOS for the d orbital of **RHO**-Cu(I) and **RHO**-Cu(II). The H, O, Al, Si, P, and Cu atoms are represented by white, red, magenta, yellow, blue, and orange spheres.

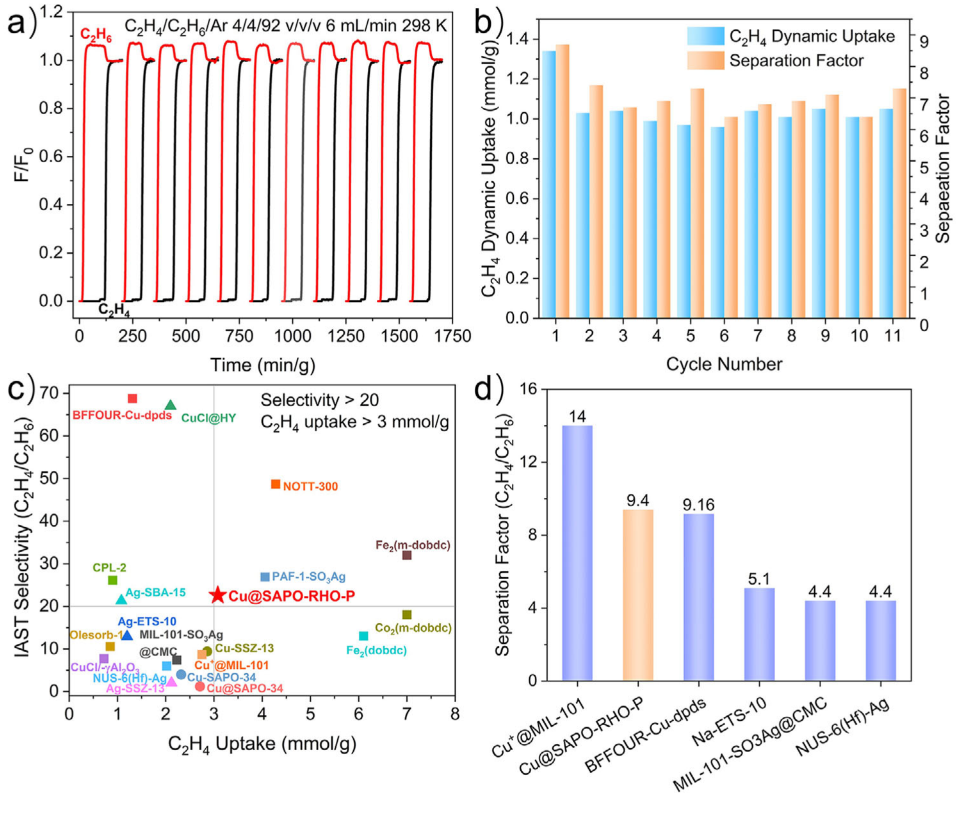

Figure 5. a) C_2H_4/C_2H_6/Ar (4/4/92, v/v/v, 6 mL min^{-1}) breakthrough cycles for Cu@SAPO-RHO-P at 298 K and 1 bar with the regeneration at 298 K for 30 min, b) C_2H_4 dynamic uptake and C_2H_4/C_2H_6 separation factor during breakthrough cycles with the regeneration at 298 K for 30 min, comparison of c) IAST selectivity of the mixture of C_2H_4/C_2H_6 and the static C_2H_4 uptake based on equilibrium effect and d) C_2H_4/C_2H_6 dynamic separation factor under ambient conditions for state-of-the-art adsorbent materials.

at higher C_2H_4/C_2H_6 concentrations (Figure S28). These results demonstrated that Cu@SAPO-RHO-P maintained exceptional performance under varying gas compositions, flow rates, humidity levels, and temperatures, highlighting its potential for industrial applications.

To simulate industrial conditions, a typical cracked gas mixture (C_2H_4/C_2H_6, 15/1, v/v)[26] was used instead of pure C_2H_4 during pretreatment. This adjustment also improved the separation performance, achieving a dynamic C_2H_4 uptake of 1.33 mmol g^{-1} and a separation factor of 8.4 under ambient conditions over five fully regenerable breakthrough cycles (C_2H_4/C_2H_6/Ar, 4/4/92, v/v/v) (Figure S29).

Additionally, carbon species formed during C_2H_4 pretreatment reduced water vapor adsorption by 65.53 mg g^{-1} (Figure S30), thereby improving the material's water resistance and practicality in humid environments.[9] The enhanced water resistance, induced by carbon species, also stabilized Cu(I) by partially blocking water from entering the zeolite microchannel.[41] Long-term stability tests showed that Cu@SAPO-RHO-P retained 87% of its C_2H_4 dynamic uptake capacity after 8 months of ambient storage with silica gel, compared to 60% for H-SAPO-RHO (Figure S31).

Given that IAST does not consider steric effect in confined pore systems, and kinetic selectivity is emphasized for evaluating kinetic-based separation performance,[4] Figure 5c compares Cu@SAPO-RHO-P with state-of-the-art adsorbents in terms of IAST selectivity for C_2H_4/C_2H_6 and static C_2H_4 uptake under ambient equilibrium-based conditions (Table S6). Cu@SAPO-RHO-P demonstrated both high selectivity (> 20) and C_2H_4 adsorption capacity (> 3 mmol g^{-1}), positioning it among the top-performing zeolite adsorbents. Moreover, Figure 5d highlights its superior dynamic separation performance, which is more representative of practical applications. These results highlight the potential of Cu@SAPO-RHO-P for industrial-scale C_2H_4/C_2H_6 separations.

Conclusion

In summary, Cu@SAPO-RHO zeolite was directly synthesized for the first time using a simple one-pot method with cyclam as the Cu(II) ligand. The Cu content was adjustable by modulating the initial gel composition, overcoming the limitations of Cu content in Cu-SAPO-RHO prepared via ion-exchange or CuO/SAPO-RHO via wet impregnation. After C_2H_4 pretreatment, the material exhibited excellent C_2H_4/C_2H_6 separation performance, with a dynamic separation factor of 9.4 and a C_2H_4 retention time of 120 min g^{-1} at 298 K and 1 bar. These results position Cu@SAPO-RHO among the best-performing zeolite adsorbents for this application.

Structural analysis through Rietveld refinement revealed that Cu^{2+} ions occupy the corners of elliptical single 8-rings (*s8r*). The C_2H_4 pretreatment partially reduced Cu(II) to Cu(I), which selectively enhanced C_2H_4 adsorption, increasing static C_2H_4 uptake from 2.76 to 3.08 mmol g^{-1}. This reduction was confirmed by XANES, XPS, and EPR analyses, and was accompanied by an increase in the heat of adsorption for C_2H_4, as indicated by temperature-dependent adsorption isotherms. DFT calculations further supported these observations, showing a stronger adsorption affinity between Cu(I) and C_2H_4. The optimal Cu content in Cu@SAPO-RHO was critical for achieving maximum separation efficiency after C_2H_4 pretreatment. Additionally, carbon species formed during C_2H_4 pretreatment enhanced water resistance, further improving the material's suitability for industrial applications.

Overall, Cu@SAPO-RHO zeolite, with its simple synthesis, low production cost, and significantly enhanced separation efficiency after C_2H_4 pretreatment, demonstrates excellent potential for industrial C_2H_4/C_2H_6 separation. The C_2H_4 pretreatment strategy offers valuable insights for designing efficient and robust adsorptive separation processes suitable for practical applications.

Acknowledgements

The authors thank the National Key Research and Development Program of China (Grant 2021YFA1501202), the National Natural Science Foundation of China (Grant 22288101, 22102177, 22372156), and the '111 Center' (B17020) for supporting this work. Beamline BL14W1 of the Shanghai Synchrotron Radiation Facility (SSRF, China) is acknowledged for providing the beamtime.

Conflict of Interests

The authors declare no conflict of interest.

Data Availability Statement

The data that support the findings of this study are available from the corresponding author upon reasonable request.

Keywords: Adsorptive separation • C_2H_4 pretreatment • C_2H_4/C_2H_6 separation • Cu • SAPO-RHO zeolite

---

[1] M. Bajus, V. Veselý, P. A. Leclercq, J. A. Rijks, *Ind. Eng. Chem. Prod. Res. Dev.* **1980**, *19*, 556–563.
[2] Y. Gao, L. Neal, D. Ding, W. Wu, C. Baroi, A. M. Gaffney, F. Li, *ACS Catal.* **2019**, *9*, 8592–8621.
[3] S. Matar, L. F. Hatch in *Chemistry of Petrochemical Processes (Second Edition)* (Eds.: S. Matar, L. F. Hatch), Gulf Professional Publishing, Woburn, **2001**, pp. 49–110.
[4] E. Pérez-Botella, S. Valencia, F. Rey, *Chem. Rev.* **2022**, *122*, 17647–17695.
[5] Y. Li, J. Yu, *Nat. Rev. Mater.* **2021**, *6*, 1156–1174.
[6] D. S. Sholl, R. P. Lively, *Nature* **2016**, *532*, 435–437.
[7] M. Rungta, C. Zhang, W. J. Koros, L. Xu, *AIChE J.* **2013**, *59*, 3475–3489.
[8] R. Bai, X. Song, W. Yan, J. Yu, *Natl. Sci. Rev.* **2022**, *9*, nwac064.
[9] Q. Ke, F. Xiong, G. Fang, J. Chen, X. Niu, P. Pan, G. Cui, H. Xing, H. Lu, *Adv. Mater.* **2024**, *36*, 2408416.
[10] Y. Wang, S. B. Peh, D. Zhao, *Small* **2019**, *15*, 1900058.
[11] Y. Wu, B. M. Weckhuysen, *Angew. Chem. Int. Ed.* **2021**, *60*, 18930–18949.
[12] S. Aguado, G. Bergeret, C. Daniel, D. Farrusseng, *J. Am. Chem. Soc.* **2012**, *134*, 14635–14637.
[13] Z. Bao, J. Wang, Z. Zhang, H. Xing, Q. Yang, Y. Yang, H. Wu, R. Krishna, W. Zhou, B. Chen, Q. Ren, *Angew. Chem. Int. Ed.* **2018**, *57*, 16020–16025.
[14] H. S. Lee, N. S. Kim, D. Kwon, S.-K. Lee, M. Numan, T. Jung, K. Cho, M. Mazur, H. S. Cho, C. Jo, *Adv. Mater.* **2021**, *33*, 2105398.
[15] P. J. Bereciartua, Á. Cantín, A. Corma, J. L. Jordá, M. Palomino, F. Rey, S. Valencia, E. W. Corcoran, P. Kortunov, P. I. Ravikovitch, A. Burton, C. Yoon, Y. Wang, C. Paur, J. Guzman, A. R. Bishop, G. L. Casty, *Science* **2017**, *358*, 1068–1071.

[16] J. E. Bachman, M. T. Kapelewski, D. A. Reed, M. I. Gonzalez, J. R. Long, *J. Am. Chem. Soc.* **2017**, *139*, 15363–15370.

[17] E. D. Bloch, W. L. Queen, R. Krishna, J. M. Zadrozny, C. M. Brown, J. R. Long, *Science* **2012**, *335*, 1606–1610.

[18] S. Yang, A. J. Ramirez-Cuesta, R. Newby, V. Garcia-Sakai, P. Manuel, S. K. Callear, S. I. Campbell, C. C. Tang, M. Schröder, *Nat. Chem.* **2015**, *7*, 121–129.

[19] Q. Ding, Z. Zhang, C. Yu, P. Zhang, J. Wang, X. Cui, C.-H. He, S. Deng, H. Xing, *Sci. Adv.* **2020**, *6*, eaaz4322.

[20] R.-B. Lin, L. Li, H.-L. Zhou, H. Wu, C. He, S. Li, R. Krishna, J. Li, W. Zhou, B. Chen, *Nat. Mater.* **2018**, *17*, 1128–1133.

[21] Y Peng, H Xiong, P Zhang, Z Zhao, X Liu, S Tang, Y Liu, Z Zhu, W Zhou, Z Deng, J Liu, Y Zhong, Z Wu, J Chen, Z Zhou, S Chen, S Deng, J Wang, *Nat. Commun.* **2024**, *15*, 625.

[22] B. Li, Y. Zhang, R. Krishna, K. Yao, Y. Han, Z. Wu, D. Ma, Z. Shi, T. Pham, B. Space, J. Liu, P. K. Thallapally, J. Liu, M. Chrzanowski, S. Ma, *J. Am. Chem. Soc.* **2014**, *136*, 8654–8660.

[23] N. Kumar, S. Mukherjee, N. C. Harvey-Reid, A. A. Bezrukov, K. Tan, V. Martins, M. Vandichel, T. Pham, L. M. van Wyk, K. Oyekan, A. Kumar, K. A. Forrest, K. M. Patil, L. J. Barbour, B. Space, Y. Huang, P. E. Kruger, M. J. Zaworotko, *Chem* **2021**, *7*, 3085–3098.

[24] H. Yu, J. Zang, C. Guo, B. Li, B. Li, X. Zhang, T. Chen, *Separations* **2023**, *10*, 17.

[25] T. R. Yang in *Adsorbents: Fundamentals and Applications*, John Wiley & Sons, Hoboken, **2003**, pp. 1–7.

[26] P.-Q. Liao, W.-X. Zhang, J.-P. Zhang, X.-M. Chen, *Nat.Commun*. **2015**, *6*, 8697.

[27] T. R. Yang in *Adsorbents: Fundamentals and Applications*, John Wiley & Sons, Hoboken, **2003**, pp. 191–230.

[28] S. U. Rege, J. Padin, R. T. Yang, *AIChE J.* **1998**, *44*, 799–809.

[29] S. Uchida, R. Kawamoto, H. Tagami, Y. Nakagawa, N. Mizuno, *J. Am. Chem. Soc.* **2008**, *130*, 12370–12376.

[30] Y.-Y. Huang, *J. Catal.* **1980**, *61*, 461–476.

[31] A. Van Miltenburg, W. Zhu, F. Kapteijn, J. A. Moulijn, *Chem. Eng. Res. Des.* **2006**, *84*, 350–354.

[32] J. G. Min, K. C. Kemp, S. B. Hong, *Sep. Purif. Technol.* **2020**, *250*, 117146.

[33] Z. Li, K. Xie, R. C. T. Slade, *Appl. Catal. A: Gen.* **2001**, *209*, 107–115.

[34] V. Magné, T. Garnier, M. Danel, P. Pale, S. Chassaing, *Org. Lett.* **2015**, *17*, 4494–4497.

[35] S. Shwan, M. Skoglundh, L. F. Lundegaard, R. R. Tiruvalam, T. V. W. Janssens, A. Carlsson, P. N. R. Vennestrøm, *ACS Catal.* **2015**, *5*, 16–19.

[36] H. Chen, M. Matsuoka, J. Zhang, M. Anpo, *J. Catal.* **2004**, *228*, 75–79.

[37] M. Occhiuzzi, G. Fierro, G. Ferraris, G. Moretti, *Chem. Mater.* **2012**, *24*, 2022–2031.

[38] E. Borfecchia, K. A. Lomachenko, F. Giordanino, H. Falsig, P. Beato, A. V. Soldatov, S. Bordiga, C. Lamberti, *Chem. Sci.* **2015**, *6*, 548–563.

[39] S. Phutthapatimok, P. Sridechparsat, P. Rangsunvigit, S. Kulprathipanja, *Chiang Mai J. Sci.* **2016**, *43*, 590–598.

[40] G. Li, H. Wang, Q. Li, X. Zhang, Y. Qin, Y. Bi, L. Song, *New J. Chem.* **2023**, *47*, 5650–5658.

[41] Y.-X. Li, J.-X. Shen, S.-S. Peng, J.-K. Zhang, J. Wu, X.-Q. Liu, L.-B. Sun, *Nat. Commun.* **2020**, *11*, 3206.

[42] J.-X. Qin, Z.-M. Wang, X.-Q. Liu, Y.-X. Li, L.-B. Sun, *J. Mater. Chem. A* **2015**, *3*, 12247–12251.

[43] S. Shi, Y.-X. Li, S.-S. Li, X.-Q. Liu, L.-B. Sun, *Green Energy Environ.* **2022**, *7*, 345.

[44] Z. Zhang, Y. Liu, Y. T. Hu, S. Gu, J. Wang, Y. Shen, P. Li, *Microporous Mesoporous Mater.* **2023**, *350*, 112450.

[45] Y. Xiao, Q. Guo, S. Yang, Q. Zhao, G. He, *ACS Sustainable Chem. Eng.* **2024**, *12*, 12446–12456.

[46] S. Moussa, P. Concepción, M. A. Arribas, A. Martínez, *ACS Catal.* **2018**, *8*, 3903–3912.

[47] L. Yang, C. Wang, L. Zhang, W. Dai, Y. Chu, J. Xu, G. Wu, M. Gao, W. Liu, Z. Xu, P. Wang, N. Guan, M. Dyballa, M. Ye, F. Deng, W. Fan, L. Li, *Nat. Commun.* **2021**, *12*, 4661.

[48] J. Zhong, J. Han, Y. Wei, Z. Liu, *J. Catal.* **2021**, *396*, 23–31.

[49] W. Zhang, S. Lin, Y. Wei, P. Tian, M. Ye, Z. Liu, *Natl. Sci. Rev.* **2023**, *10*, nwad120.

[50] X. Su, P. Tian, J. Li, Y. Zhang, S. Meng, Y. He, D. Fan, Z. Liu, *Microporous Mesoporous Mater.* **2011**, *144*, 113–119.

[51] X. Wang, N. Yan, M. Xie, P. Liu, P. Bai, H. Su, B. Wang, Y. Wang, L. Li, T. Cheng, P. Guo, W. Yan, J. Yu, *Chem. Sci.* **2021**, *12*, 8803–8810.

[52] A. Garsuch, O. Klepel, *Carbon* **2005**, *43*, 2330–2337.

[53] M. Chen, J. Li, W. Xue, S. Wang, J. Han, Y. Wei, D. Mei, Y. Li, J. Yu, *J. Am. Chem. Soc.* **2022**, *144*, 12816–12824.

[54] N. Yan, L. Wang, X. Liu, P. Wu, T. Sun, S. Xu, J. Han, P. Guo, P. Tian, Z. Liu, *J. Mater. Chem. A* **2018**, *6*, 24186–24193.

[55] C. Y. Lee, Y.-S. Bae, N. C. Jeong, O. K. Farha, A. A. Sarjeant, C. L. Stern, P. Nickias, R. Q. Snurr, J. T. Hupp, S. T. Nguyen, *J. Am. Chem. Soc.* **2011**, *133*, 5228–5231.

[56] J. Kärger, D. M. Ruthven, D. N. Theodorou, in *Diffusion in Nanoporous Materials*, Wiley-VCH Verlag & Co. KGaA, Weinheim, **2012**, pp. 427–457.

[57] S Liu, X Han, Y Chai, G Wu, W Li, J Li, I Da Silva, P Manuel, Y Cheng, L L. Daemen, A J. Ramirez-Cuesta, W Shi, N Guan, S Yang, L Li, *Angew. Chem. Int. Ed.* **2021**, *60*, 6526–6532.

[58] P. Kappen, J.-D. Grunwaldt, B. S. Hammershøi, L. Tröger, B. S. Clausen, *J. Catal.* **2001**, *198*, 56–65.

[59] D. Grandjean, H. L. Castricum, J. C. van den Heuvel, B. M. Weckhuysen, *J. Phys. Chem. B* **2006**, *110*, 16892–16901.

[60] J. G. Mesu, A. M. Beale, F. M. F. de Groot, B. M. Weckhuysen, *J. Phys. Chem. B* **2006**, *110*, 17671–17677.

[61] T. Magadzu, J.-K. Yang, J. D. Henao, M. C. Kung, H. H. Kung, M. S. Scurrell, *J. Phys. Chem. C* **2017**, *121*, 8812–8823.

[62] P. Zhan, J. Zhuang, S. Yang, X. Li, X. Chen, T. Wen, L. Lu, P. Qin, B. Han, *Angew. Chem. Int. Ed.* **2024**, *63*, e202409019.

[63] L. Meda, G. Ranghino, G. Moretti, G. F. Cerofolini, *Surf. Interface Anal.* **2002**, *33*, 516–521.

[64] A. Quindimil, U. De-La-Torre, B. Pereda-Ayo, J. A. González-Marcos, J. R. González-Velasco, *Appl. Catal. B: Environ.* **2018**, *238*, 393–403.

[65] K. Qian, W. Tian, L. Yin, Z. Yang, F. Tian, D. Chen, *Appl. Catal. B: Environ.* **2023**, *339*, 123159.

[66] A. Takahashi, R. T. Yang, C. L. Munson, D. Chinn, *Langmuir* **2001**, *17*, 8405–8413.

[67] C. C. Chusuei, M. A. Brookshier, D. W. Goodman, *Langmuir* **1999**, *15*, 2806–2808.

[68] Y. Xie, Y. Yin, S. Zeng, M. Gao, H. Su, *Catal. Commun.* **2017**, *99*, 110–114.

[69] M. Chen, W. Zhao, Y. Wei, S.-B. Ren, Y. Chen, D. Mei, D.-M. Han, J. Yu, *Chem. Sci.* **2024**, *15*, 5548–5554.

[70] T. Nanba, S. Masukawa, A. Ogata, J. Uchisawa, A. Obuchi, *Appl. Catal. B: Environ.* **2005**, *61*, 288–296.

[71] U. Deka, I. Lezcano-Gonzalez, B. M. Weckhuysen, A. M. Beale, *ACS Catal.* **2013**, *3*, 413–427.

[72] G. Fu, R. Yang, Y. Liang, X. Yi, R. Li, N. Yan, A. Zheng, L. Yu, X. Yang, J. Jiang, *Microporous Mesoporous Mater.* **2021**, *320*, 111060.

[73] B. Hammer, J. K. Nørskov, *Adv. Catal.*, **2000**, *45*, 71–129.

Manuscript received: January 14, 2025
Revised manuscript received: March 16, 2025
Accepted manuscript online: March 17, 2025
Version of record online: March 31, 2025